

Advancing Characterization of Materials by Multimodal 4D-STEM Analytical Methods

April 26, 11:00am - 12:00pm EDT

Development and production of new materials and semiconductor devices require morphological, structural, and chemical characterization at the nanoscale level to understand their chemico-physical properties and optimize their production process. Besides traditional electron microscopy imaging and compositional analysis techniques, 4D-STEM methods provide additional structural information about the local internal organization of atoms and molecules at each position of an acquired STEM map.

Watch this session during the WAS Virtual Conference:



Dr. Daniel Nemecek



Dr. Tingting Yang

[Register Now](#)

Physio-Electrochemically Durable Dry-Processed Solid-State Electrolyte Films for All-Solid-State Batteries

Dong Ju Lee, Jihyun Jang, Jung-Pil Lee, Junlin Wu, Yu-Ting Chen, John Holoubek, Kunpeng Yu, So-Yeon Ham, Yuju Jeon, Tae-Hee Kim, Jeong Beom Lee, Min-Sang Song, Ying Shirley Meng, and Zheng Chen*

The dry process is a promising fabrication method for all-solid-state batteries (ASSBs) to eliminate energy-intensive drying and solvent recovery steps and to prevent degradation of solid-state electrolytes (SSEs) in the wet process. While previous studies have utilized the dry process to enable thin SSE films, systematic studies on their fabrication, physical and electrochemical properties, and electrochemical performance are unprecedented. Here, different fabrication parameters are studied to understand polytetrafluoroethylene (PTFE) binder fibrillation and its impact on the physio-electrochemical properties of SSE films, as well as the cycling stability of ASSBs resulting from such SSEs. A counter-balancing relation between the physio-electrochemical properties and cycling stability is observed, which is due to the propagating behavior of PTFE reduction (both chemically and electrochemically) through the fibrillation network, resulting in cell failure from current leakage and ion blockage. By controlling PTFE fibrillation, a bilayer configuration of SSE film to enable physio-electrochemically durable SSE film for both good cycling stability and charge storage capability of ASSBs is demonstrated.

the manner in which they are integrated into one device have lagged.^[17–20] In the fabrication of LIBs, the polymeric binder is indispensable, forming a physical network among the electrode materials, conductive additives, and current collector and supporting them during cell assembly.^[21,22] Likewise, manufacturing ASSBs will inevitably need a polymeric binder. However, unlike in LIBs where the polymeric binder swells in the liquid electrolyte and enables ion transport through the binder domain,^[23] the binder in ASSBs merely hinders physical contacts among active materials, conductive carbon, and solid-state electrolyte (SSE) particles. If improperly integrated, this polymer binder can block electron and ion transport pathways, increasing cell impedance and decreasing utilization of active materials.^[24,25]

Of note, processing an SSE layer in ASSBs requires more rigorous stand-


ards from cell performance and manufacturing perspectives to replace the role of liquid electrolyte and polymeric separators in LIBs. From a cell performance perspective, the SSE layer must be ion conducting and electron insulating for good cyclability as well as thin for low impedance and high energy density. From a manufacturing perspective, it should be mechanically flexible and durable enough to enable roll-to-roll process and z-folding, common techniques used in cell assembly.^[22] These two rigorous benchmarks make fabricating

1. Introduction

All-solid-state batteries (ASSBs) are considered as a promising future energy storage system with much improved safety relative to conventional lithium-ion batteries (LIBs) owing to their less flammable solid inorganic electrolytes.^[1,2] Although extensive research progress has been made on the electrolyte materials,^[3–6] cathode and anode,^[7–12] and the interface between them,^[13–16] studies on manufacturing methodologies to improve

D. J. Lee, J. Jang, J. Holoubek, Y. Jeon, T.-H. Kim, Y. S. Meng, Z. Chen
Department of NanoEngineering
University of California, San Diego
La Jolla, CA 92093, USA
E-mail: zhengchen@eng.ucsd.edu

J. Jang
Department of Chemistry
Sogang University
35 Baekbeom-ro, Mapo-gu, Seoul 04107, Republic of South Korea
J.-P. Lee, J. B. Lee, M.-S. Song
LG Energy Solution, Ltd.
LG Science Park, Magokjungang 10-ro, Gangseo-gu, Seoul 07796,
Republic of South Korea

 The ORCID identification number(s) for the author(s) of this article can be found under <https://doi.org/10.1002/adfm.202301341>.

J. Wu, Y.-T. Chen, S.-Y. Ham, Y. S. Meng, Z. Chen
Program of Materials Science and Engineering
University of California, San Diego
La Jolla, CA 92093, USA

K. Yu, Z. Chen
Program of Chemical Engineering
University of California, San Diego
La Jolla, CA 92093, USA

Y. S. Meng
Pritzker School of Molecular Engineering
University of Chicago
Chicago, IL 60637, USA

Y. S. Meng, Z. Chen
Sustainable Power and Energy Center
University of California, San Diego
La Jolla, CA 92093, USA

DOI: 10.1002/adfm.202301341

SSE films with both good electrochemical and physical properties challenging.

Two main processing methods have been investigated for the integration of polymer binders in ASSBs: wet and dry processes. The wet process, which uses a solvent to mix polymeric binder and electrode materials to form a slurry for tape casting, is a mature technology currently used in LIB manufacturing.^[22] In the early stage, the wet process was widely studied to fabricate SSE films. It was shown that solvents with low polarity and dielectric constant, such as xylene and toluene, prevent degradation of SSE,^[26,27] and that less polar binders, such as acrylonitrile butadiene rubber (NBR) and styrene butadiene rubber (SBR), are compatible with such solvents.^[28,29] Furthermore, various manufacturing parameters have been studied through machine learning to form an optimal slurry condition to fabricate high-quality SSE films.^[30] However, solvent use requires an energy-intensive drying process that consumes $\approx 47\%$ of total energy consumption in overall battery manufacturing.^[31] Moreover, when utilized for ASSB manufacturing, sulfide- and halide-based SSEs are unstable with polar solvents and moisture, which results in the generation of toxic gases and decreased ionic conductivity.^[26,32,33] The incompatibility of polar solvent also limits the choice of the binders to those with poor adhesive properties, which generally require higher binder content, further impeding the interparticle contacts.^[26,28,34]

An alternative fabrication method for ASSBs is the dry process. This process eliminates the use of solvents to mix binder and electrode materials, but rather fibrillating polytetrafluoroethylene (PTFE) binder upon shearing to interweave the particles.^[35,36] In addition, the absence of solvent significantly decreases the manufacturing cost during the drying process and prevents solvent-induced degradation of SSEs. More importantly, the unique fibril morphology of the binder yields improved mechanical properties and requires much less overall binder content compared to the wet process, resulting in improved electron and ion transport.^[37] Recently, the dry process has been employed to fabricate SSE films that showed retained ionic conductivity and a thin layer comparable to that of the pristine SSEs and commercial polymeric separators, respectively.^[37–42] Despite the feasibility of dry processing SSE films, there remain limitations in the understanding of specific process design principles. i) While the reported work showed the presence of fibrils connecting SSE particles, the exact morphology and distribution of the fibrils have not been clearly probed and understood with different fabrication parameters. ii) A systematic study on both the physical and electrochemical properties of dry-processed SSE films is necessary as they are crucial for ease of manufacturing and high cell performance. iii) Though PTFE is known to be unstable in the anode,^[43] a correlation between its poor electrochemical stability and the cycling stability of dry-processed SSE films has not been elucidated. iv) Cycling performance of dry-processed SSE films is usually demonstrated with low-energy density anodes, such as LiIn^[39,41] and graphite,^[37,40] or a non-scalable interlayer.^[42] Therefore, a comprehensive understanding and evaluation of processing and properties of dry-processed SSE films and their cycling performance is necessary.

Here, we report a systematic study of the dry process for sulfide-based SSE films using Li₆PS₅Cl (LPSCl) as the

state-of-the-art Li⁺ conductor (**Figure 1**). To fabricate an SSE film, SSE powder is shear-mixed with PTFE in a mortar and pestle until it forms a dough, which is then calendared with a temperature-controlled roller to form an SSE film. To increase the degree of shearing, the film is folded in half and calendared again which is defined as one calendar loop. Four fabrication parameters having significant effects on the film quality were chosen: PTFE loading ratio, fibrillation temperature, calendar loop, and fibrillation direction. To understand how these fabrication parameters affect the physio-electrochemical properties, scanning electron microscopy (SEM) was used to observe the PTFE morphology, the tensile strength of the films was measured, and the cycling stability of Li||lithium nickel cobalt manganese oxide (NCM) and Si||NCM cells were evaluated. Moreover, X-ray photoelectron spectroscopy (XPS), Fourier-transform infrared (FT-IR), and Raman spectroscopy were employed to understand the propagating reduction behavior of PTFE in the SSE film. Finally, a bilayer configuration of physio-electrochemically durable SSE film was demonstrated with Si||NCM full-cell to highlight the correlation between PTFE fibrillation and cycling stability of ASSBs with dry-processed SSE film.

2. Results and Discussion

The physical and electrochemical properties of SSE films prepared with different fabrication parameters were evaluated by measuring the tensile strength and ionic conductivity (**Figure 2**). The SEM image and X-ray diffraction (XRD) pattern of PTFE used in this work exhibit a particle size less than 500 nm and high crystallinity (Figures S1 and S2, Supporting Information). The tensile strength was measured under Ar atmosphere (Figure S3, Supporting Information). It was shown that the tensile strength increases, and ionic conductivity gradually decreases with increasing PTFE ratio from 0.2 to 5 wt% (Figure 2a). This trend is also observed in a typical wet process, where the increased volume fraction of the binder physically upholds the particles but hinders interparticle contacts.^[44,45] To understand the binder morphology, SEM was utilized to probe PTFE inside SSE films that was isolated by dissolving SSE in water (Figure S4, Supporting Information). SEM images of isolated PTFE (Figure 2b) show that most of the PTFE maintained its pristine spherical shape (Figure S2, Supporting Information) regardless of PTFE ratios, indicating insufficient fibrillation of PTFE powders with five calendar loops. Next, the tensile strength and ionic conductivity of SSE films fabricated with a different number of calendar loops (2, 5, 10, 15, and 30 loops) were compared (Figure 2c). With the same PTFE loading, the tensile strength was found to increase with the number of calendar loops, whereas the ionic conductivity remains similar. Compared to increasing the PTFE ratio, increasing calendar loops is shown to be more effective in maintaining ionic conductivity, as an SSE film fabricated with 0.5% PTFE and 30 calendar loops exhibited a higher ionic conductivity (1.71 mS cm⁻¹ vs 1.28 mS cm⁻¹), but a comparable tensile strength (288 kPa vs 314 kPa) compared to that with 2% PTFE and five calendar loops. SEM images show that more fibrous PTFE was clearly observed with increasing calendar loops (Figure 2d). This result shows that maximizing the

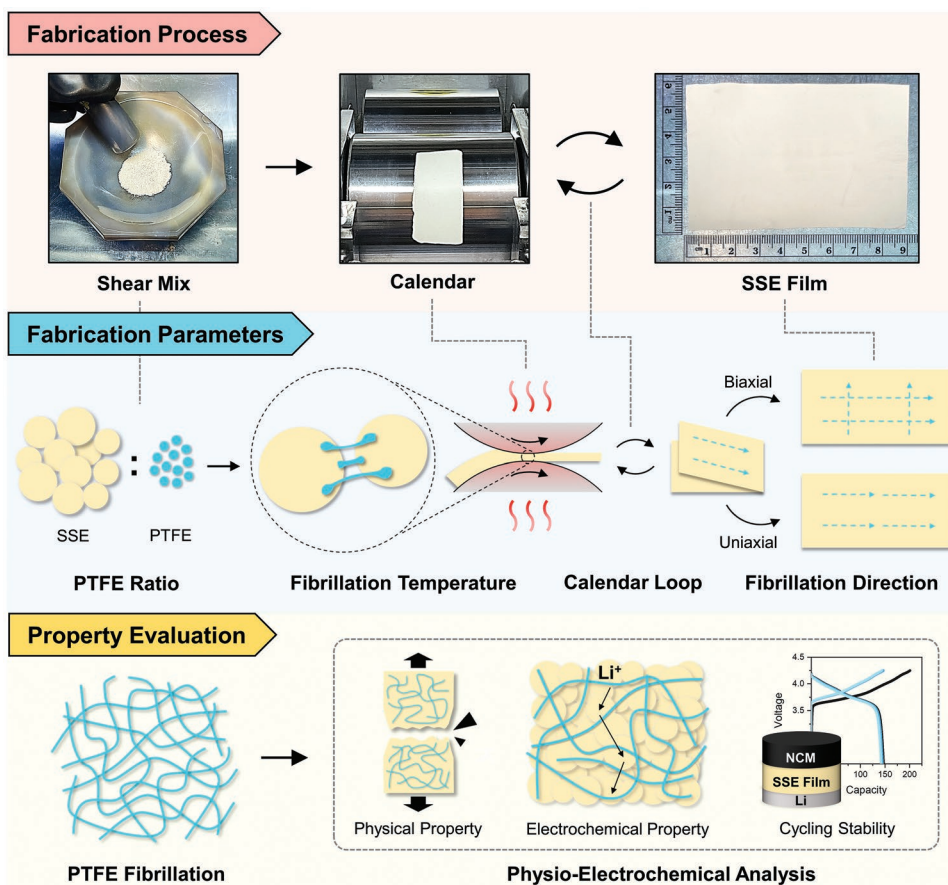


Figure 1. Schematic showing fabrication process, fabrication parameters, and property evaluation of dry-processed SSE film.

degree of fibrillation is crucial to maximizing the mechanical strength of SSE films while mitigating losses in ionic transport.

After investigating the PTFE ratios and calendaring loops, two more fibrillation conditions were studied. First, the fibrillation temperature was controlled by changing the calendaring temperature (23, 60, 90, and 120 °C) and the tensile strength of SSE films was measured (Figure 2e). It was observed that the tensile strength increases with increasing fibrillation temperature at the same number of calendar loops. SEM images of isolated PTFE show that PTFE was partially fibrillated for lower temperatures (23 and 60 °C), whereas it was fully fibrillated for higher temperatures (90 and 120 °C; Figure 2f). This trend is closely related to the temperature-dependent phase changes of PTFE, where the material has a beta transition temperature (T_{β}) of ≈ 30 °C and glass transition temperature (T_g) above 80 °C (Figure S5, Supporting Information). Thus, a fibrillation temperature above T_g of PTFE likely increases the degree of fibrillation with a fewer number of calendar loops.

Finally, the fibrillation direction, biaxial or uniaxial with respect to the previous calendar direction, was investigated. The tensile strength of SSE films fabricated with biaxial and uniaxial fibrillations was measured (Figure 2g). It was shown that both biaxially and uniaxially fibrillated SSE films have comparable tensile strength, but the uniaxially fibrillated film has a much lower tensile strength when stretched perpendicularly to its fibrillation direction. This is because aggregated 1D fibers

are formed in uniaxial fibrillation, whereas randomly dispersed fibers are formed in biaxial fibrillation as shown in SEM images (Figure 2h). In summary, the degree and uniformity of fibrillation can be increased by increasing the number of calendar loops and fibrillation temperature and with biaxial fibrillation, respectively (Figure 2i). This result indicates that unlike in wet-processed films, the physical and electrochemical properties of dry-processed films are determined not only by the binder content but also by the degree and quality of binder fibrillation.

The cycling stability of SSE films was evaluated with Li||NCM half-cells by varying the PTFE ratios (0.2% and 0.5%) and calendar loops (5 and 30 loops) and fixing the fibrillation temperature and direction to 90 °C and biaxial. The PTFE ratios of 0.2% and 0.5% were chosen, as they are commonly used in published works.^[38,40,42] Top-view SEM images of the SSE films are also shown in Figure S6 (Supporting Information). From the voltage profiles of the first three cycles, the cell assembled with 0.2%, 5 loops SSE film shows stable cycling (Figure 3a), whereas that with 0.2%, 30 loops SSE film shows decreased discharge capacities (Figure 3b). In addition, the second and the third charge capacities were higher than the first discharge capacity as indicated by the black dashed line, and this unusual trend was aggravated in the cell with 0.5%, 5 loops SSE film, where the charge capacity further increased in the subsequent cycle (Figure 3c). The cell with 0.5%, 30 loops SSE film resulted in an immediate short-circuit during the first

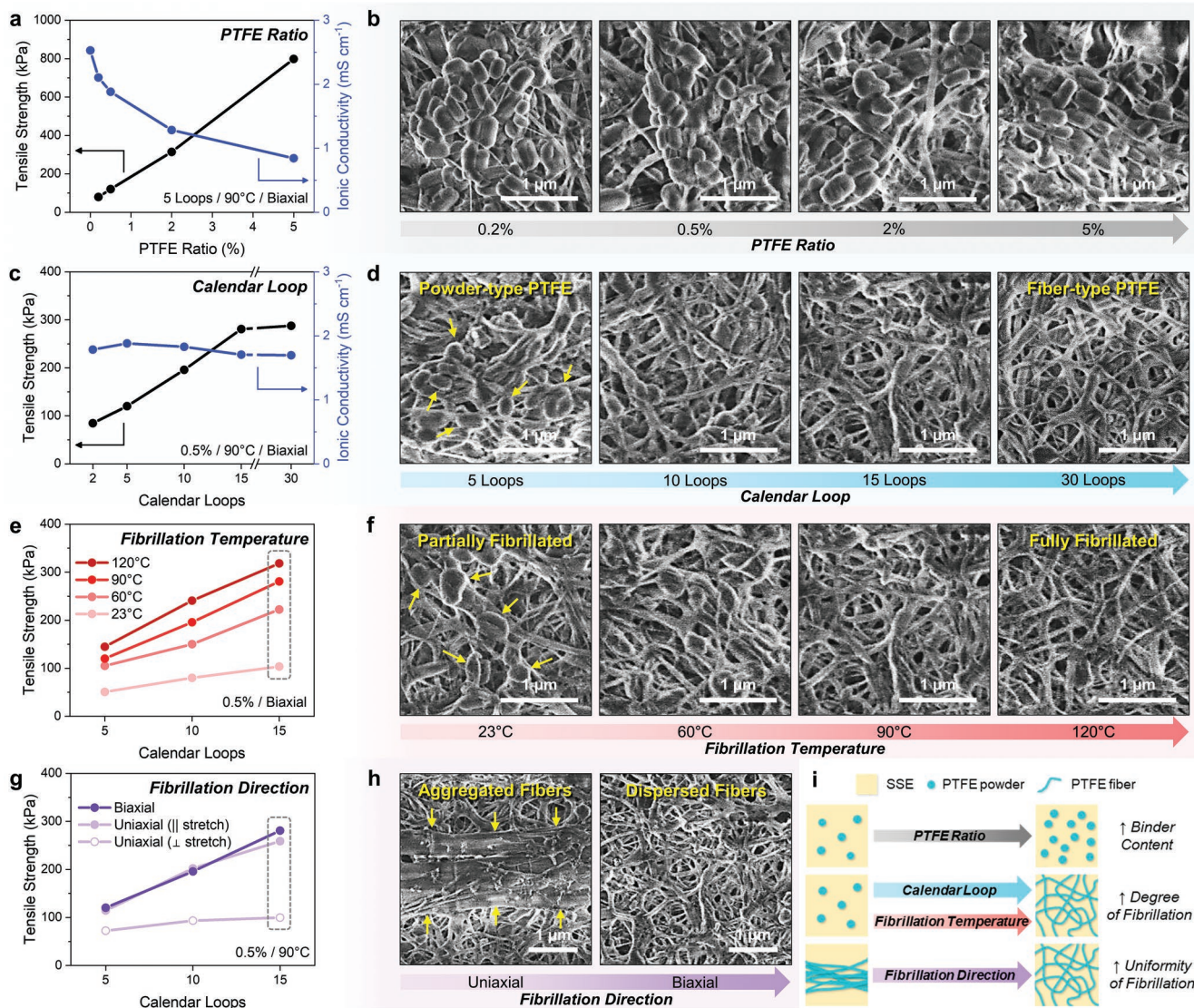


Figure 2. Evaluation of physical and electrochemical properties of SSE films. a,c) Tensile strength and ionic conductivity, and b,d) SEM images of PTFE morphology of SSE films fabricated with different PTFE ratios and calendar loops, respectively. e,g) Tensile strength and f,h) SEM images of PTFE morphology of SSE films fabricated with different fibrillation temperatures and directions, respectively. i) Schematic showing the summary of PTFE morphology with different fabrication parameters.

charging, failing to increase the cell voltage (Figure 3d). The summary of the Coulombic efficiencies (CEs) of the first three cycles of the corresponding half-cell shows that the CE of the third cycle clearly decreases with increasing PTFE ratio and calendar loops (Figure 3e). Moreover, the electrochemical impedance spectroscopy (EIS) result obtained before cycling the corresponding half-cells displays an increase in cell impedance with increasing PTFE ratio and calendar loops (Figure 3f). Furthermore, because PTFE is known to be unstable with Li metal upon contact,^[46,47] the cycling stability of SSE films was also evaluated with Si|NCM full-cells (Figure S7a–e, Supporting Information). Despite the mitigated chemical stability as shown in comparable cell impedances before cycling (Figure S7f, Supporting Information), a similar trend of cycling stability was observed. This is because PTFE is still electrochemically unstable at a low potential of ≈ 1.0 V (vs Li/Li⁺) as shown in the

cyclic voltammetry (CV) measurement (Figure S8, Supporting Information).^[43,48]

X-ray photoelectron spectroscopy (XPS) was utilized to understand the chemical changes of SSE film. An SSE film, prepared with an excess PTFE ratio of 5% to exaggerate any side reactions, was chemically reduced through contact with Li metal for 3 days. Note that complete contact with Li metal was avoided for further surface characterization after detachment. From an optical image, the surface of the film that was in contact with Li metal appeared black (Figure 4a). Surprisingly, the opposite side of the film, not in contact with Li metal, also appeared black. Top-view SEM images also show that PTFE fibers remained intact after the chemical reduction (Figure S9, Supporting Information). From C 1s spectra obtained on the black spots for both Li and cathode sides of the reduced SSE film, the C-F₂ peak, attributed to pristine PTFE, fades while C-F

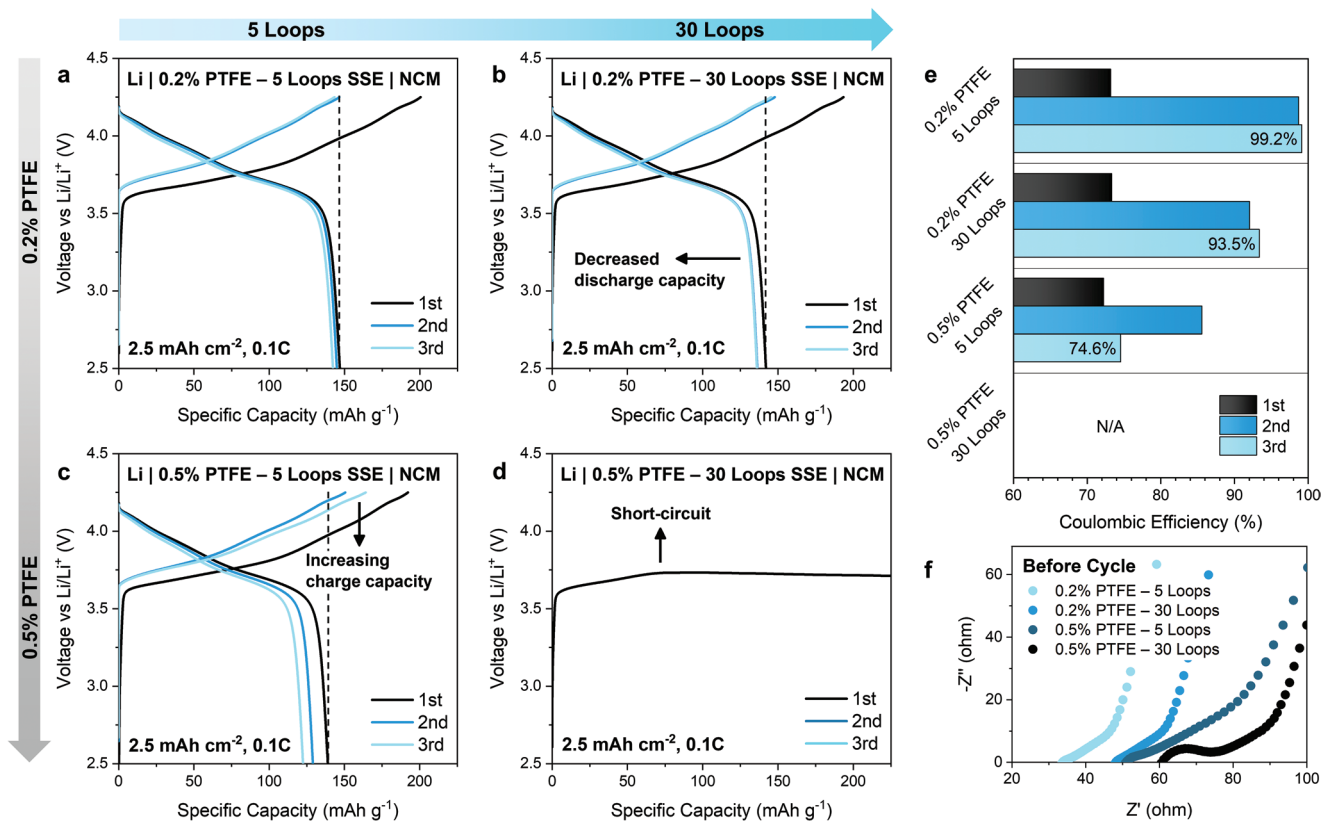


Figure 3. Evaluation of cycling stability of SSE films with Li metal anode. Voltage profiles of the first 3 cycles for Li||NCM half-cell assembled with SSE film fabricated using a) 0.2% PTFE, 5 loops, b) 0.2% PTFE, 30 loops, c) 0.5% PTFE, 5 loops, and d) 0.5% PTFE, 30 loops. Black dashed lines represent the first discharge capacity. e) CEs and f) Nyquist plots obtained before cycling of the corresponding half-cells.

and various carbon peaks are formed, indicating the defluorination of PTFE and formation of carbon species.^[49] The formation of LiF peak in F 1s spectra indicates that the defluorination of PTFE was rendered by the reduction with Li metal (Figure 4b). Furthermore, the PS_4^{3-} peak in S 2p spectra, attributed to the pristine LPSCL, fades and the Li_2S peak is formed, indicating the degradation of LPSCL (Figure 4c).^[7,13] According to this information, a proposed reduction mechanism of PTFE in SSE film is illustrated (Figure 4d). Upon the contact of PTFE with Li metal, PTFE is defluorinated to form LiF and conductive carbon species, while LPSCL contacting the carbon species is reduced to Li_2S . Moreover, electrons conduct through the reduced PTFE fibers that are formed of various conductive carbon species, and lithium ions conduct through LPSCL. As both the electron and lithium-ion conduction pathways are present, the reaction continuously propagates through PTFE fibers and eventually reaches the cathode side, which is confirmed by the same reduction species observed on the Li side.

Changes in chemical and electrochemical properties of reduced PTFE were further characterized with Fourier-transform infrared (FT-IR), Raman spectroscopy, and direct current (DC) polarization. The formation of C=C bonds in reduced PTFE from FT-IR spectroscopy (Figure 4e) and the evolution of D and G bands from Raman spectroscopy (Figure 4f) suggest that the carbon species formed after the defluorination are mostly electron-conductive sp^2 carbon species.^[50,51] These chemical changes of reduced PTFE ultimately lead to a change

in the electronic conductivity of the SSE film, where the electron conductivity of the reduced film is significantly increased compared to that of the pristine film (Figure 4g). Accordingly, two mechanisms of cell failure are illustrated (Figure 4h). First, degradation of LPSCL from reduced PTFE results in local blockage of lithium-ion transport, which was also observed from the increased cell impedance in the EIS result (cells before cycling) with increasing PTFE ratios and calendar loops (Figure 3f). Furthermore, increased electron conductivity of reduced SSE film results in current leakage. When electrons are leaked through reduced PTFE fibers during charging, the cell voltage drops and renders the cyclers to read an extra current, leading to higher charge capacities than discharge capacities (Figure 3b,c) or a failure to increase cell voltage due to an immediate short-circuit (Figure 3d).

The evaluation of physio-electrochemical properties of SSE films and their cycling stability exhibits a counter-balancing relation. An SSE film with a high degree of fibrillation is favorable to increase its mechanical strength, whereas that with a low degree of fibrillation is favorable to mitigate the propagation of PTFE reduction to prevent current leakage of SSE films. To fulfill both the physio-electrochemical properties and cycling stability, a bilayer configuration of SSE film is proposed (Figure 5a). Two bilayer SSE films, denoted by BilayerSSE-1 and BilayerSSE-2, were fabricated. BilayerSSE-1 has a physically durable layer (0.5% PTFE, 30 loops) on the cathode side and an electrochemically durable layer (0.2% PTFE, 5 loops) on the anode side,

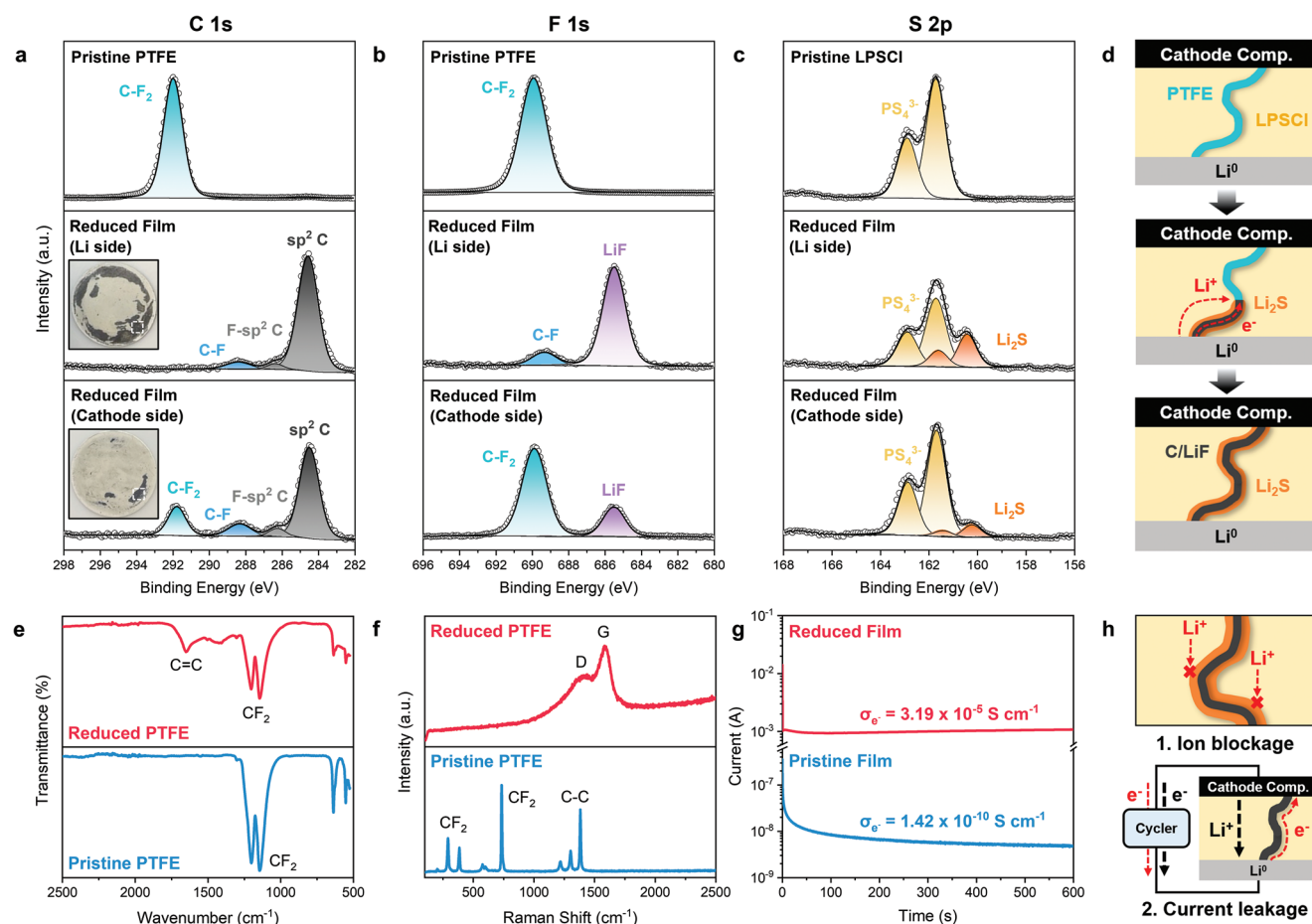


Figure 4. a) C 1s, b) F 1s, and c) S 2p XPS of dry-processed SSE films at their pristine and reduced states. The spectra of both the Li and cathode sides of the reduced SSE film are collected. d) Schematic showing a proposed reduction mechanism of PTFE in SSE film contacting Li metal. e) FT-IR and f) Raman spectra of pristine and reduced PTFE, and g) DC polarization of reduced and pristine film. h) Schematic showing proposed mechanisms of cell failure.

while BilayerSSE-2 has the same physically durable layer on the cathode side but an electrochemically vulnerable layer (0.2% PTFE, 30 loops) on the anode side. The voltage profiles and CEs of Li||NCM half-cells assembled with the bilayer configurations show a clear difference, where the cell with BilayerSSE-1 shows more retained discharge capacities and higher CEs compared to those of BilayerSSE-2 (Figure S10a–d, Supporting Information). Nevertheless, both cells short-circuited within 40 cycles due to the intrinsic dendrite issue of the Li metal anode, making it difficult to evaluate their long-term cycling performance (Figure S10e, Supporting Information). This shorting issue related to Li metal anode remains a critical issue to be addressed in building ASSBs but cannot be addressed simply with composite SSEs.

To mitigate this issue, the Si anode was found to be compatible with dry-processed SSE film. From the voltage profiles of the first three cycles and CEs of Si||NCM full-cells, the cell with BilayerSSE-1 also showed better cycling stability than that with BilayerSSE-2 (Figure 5b–e). The long-term cycling performance of the corresponding full-cells was evaluated at 0.33C (Figure 5f). The average CE of BilayerSSE-1 was higher than that of BilayerSSE-2 (99.7% vs 97.9%), but the difference in their

discharge capacities was negligible, both showing $\approx 70\%$ capacity retention after 200 cycles. However, the current leakage issue became more apparent in charge storage capability. The shelf-life test was conducted on the full-cells at various resting durations. The normalized discharge capacities of the cell with BilayerSSE-2 dramatically decreased after the rest compared to that with BilayerSSE-1 (0.93 vs 0.81 after 2 days of rest) (Figure 5g). The cell voltage of the cell with BilayerSSE-2 also noticeably declined compared to that with BilayerSSE-1 (4.04 V vs 3.92 V after 20 h of rest) (Figure 5h). This result indicates that the current leakage issue due to PTFE reduction in SSE films becomes more apparent in the calendar life capability of the cell.

3. Conclusion

In summary, the effect of PTFE fibrillation on the physical and electrochemical properties of dry-processed SSE films and the cycling stability of ASSBs was systematically studied. The tensile strength and ionic conductivity of SSE films prepared with different fabrication parameters (PTFE ratio, calendar loops, fibrillation temperature, and fibrillation direction) were

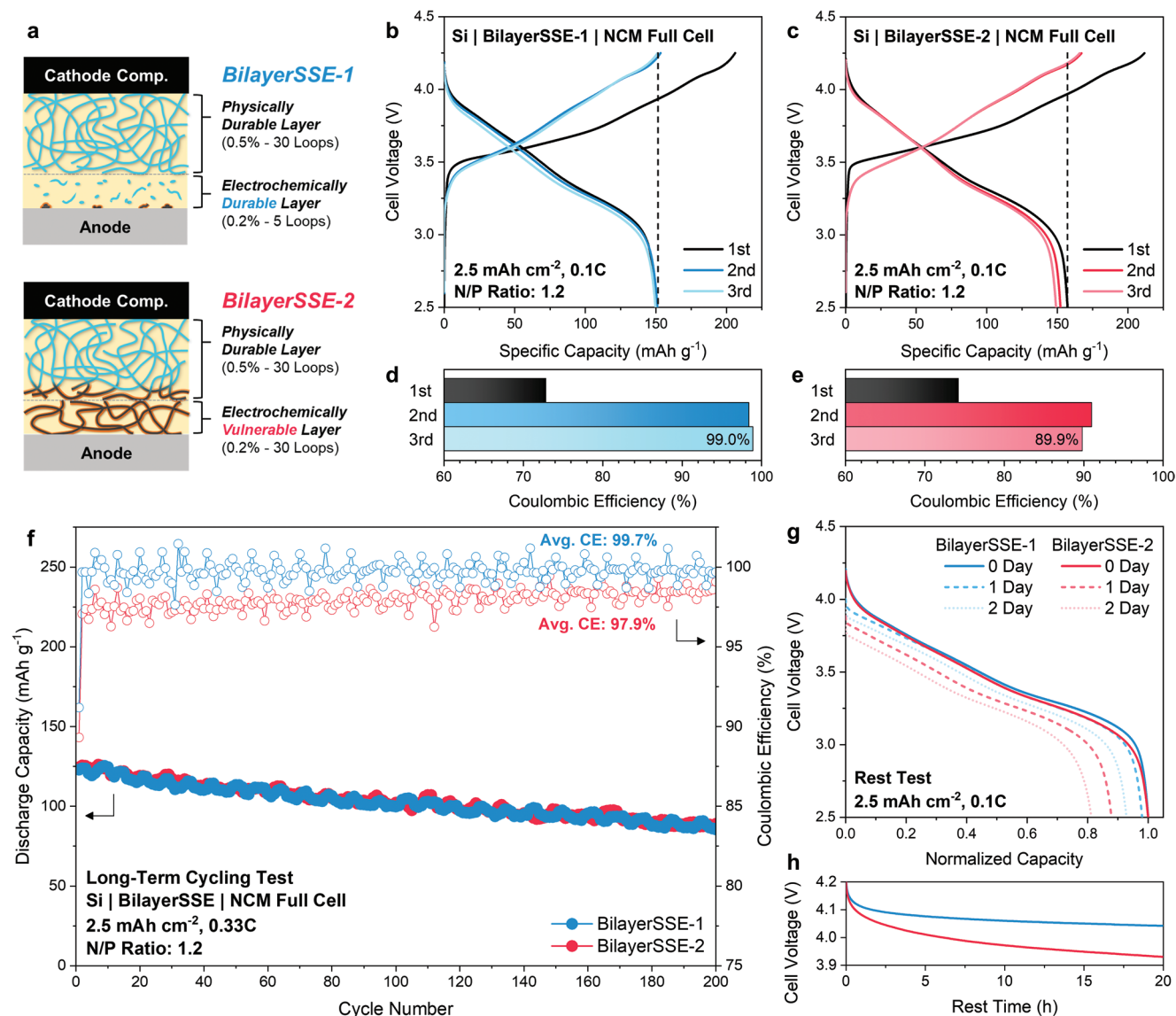


Figure 5. a) Schematic showing two cell configurations of bilayer SSE films. b,c) Voltage profiles and d,e) first three-cycle CEs of Si||NCM full-cell assembled with BilayerSSE-1 and BilayerSSE-2, respectively. Black dashed lines represent the first discharge capacity. f) Long-term cycling and rest tests showing g) discharge capacity and h) voltage drop of the full-cells assembled with the bilayer SSE film. Note that the capacity fluctuation is due to changes in ambient temperature during the test.

measured, and Li||NCM half-cells were assembled. It was found that PTFE fibrillation is crucial to increase the tensile strength while maintaining the ionic conductivity of SSE film; however, increasing the degree of fibrillation yields inferior cycling stability. This is because of the propagating behavior of PTFE reduction (both chemically and electrochemically) through the network of PTFE fibers in SSE film, which results in cell failure due to current leakage and ion blockage. To compensate for the counter-balancing relation between the physio-electrochemical properties of SSE film and the cycling stability of ASSB, a bilayer configuration of physio-electrochemically durable SSE films was demonstrated to further emphasize the importance of PTFE fibrillation on cycling stability as well as charge storage capability of ASSBs. This work provides a comprehensive examination of physical and electrochemical properties

of dry-processed SSE films and their cycling performance in ASSBs. The insights obtained from this study could be leveraged to design ASSB architectures with improved cycling stability and shelf life.

4. Experimental Section

Material Preparation: $\text{Li}_6\text{PS}_5\text{Cl}$ (LPSCI, NEI Corporation, USA) and polytetrafluoroethylene (PTFE, Supporting Information, Figure S2) were used as received from the vendor for SSE films. LPSCI was further ball-milled using Emax high-energy ball mill machine (Retsch, Germany) in a zirconia jar with zirconia balls sealed under an Ar atmosphere to reduce the particle size for cathode composite. Lithium nickel cobalt manganese oxide (NCM811, LG Chem, Republic of Korea) protected with a boron-based coating was used as received. Vapor-grown carbon

fiber (VGCF, >98%, Sigma–Aldrich, USA) and acetylene black (AB, Strem Chemicals, USA) were used as received. The lithium metal chip (Canrd, China) was scratched to remove a surface oxide layer before use. Si powder (99.9% metal basis purity, Alfa Aesar, USA) was dispersed in isopropyl alcohol (VWR, USA) and drop-casted on an unfurnished side of copper foil for Si anode.

SSE Film Preparation: LPSCI and PTFE were gently shear-mixed in a mortar and pestle with the desired weight ratio until a dough was formed. The dough was calendared to form a film with a calendar machine (TMAXCN, China) at the desired fibrillation temperature. The roller gap was gradually decreased from 600 to 300 μm for every rotation of the roller. For each calendar loop, the film was detached from the roller, folded in half, and calendared again to the desired fibrillation direction with the roller gap from 600 to 300 μm . Reduced SSE films were obtained by placing one layer of SSE film fabricated with 5 wt% PTFE, five calendar loops, 90 $^{\circ}\text{C}$, and biaxial fibrillation in a 13 mm polyether ether ketone (PEEK) die and pressed at 370 MPa for 3 min with titanium plungers. Later, Li metal was placed on one side of the film, stacked with titanium plungers, and rested for 3 days without external pressure. Afterward, Li metal was detached from the SSE film for characterization. To study PTFE morphology, scanning electron microscopy (SEM) samples were prepared by attaching SSE films to carbon tape, soaking them in water to dissolve LPSCI, and vacuum-drying at room temperature to remove water. Reduced PTFE was prepared by spreading PTFE powder on Li metal and gently roll-pressing them until the color of PTFE turned black. Then, it was soaked in water to remove Li metal, and the remaining black flakes were collected and dried overnight for characterization.

Materials Characterization: SEM was collected using FEI Apreo and Scios Dual-beam. Thermal gravimetric analysis and differential scanning calorimetry (TGA/DSC) were collected using NETZSCH STA 449 F3 Jupiter Simultaneous Thermal Analyzer with Coupled QMS 403 D Aëolos Mass Spectrometer. Tensile strength was collected using a MARK-10 M5-05 force sensor by measuring a force at a fracture and dividing it by a cross-sectional area of the film. X-ray photoelectron spectroscopy (XPS) was collected using the AXIS Supra XPS by Kratos Analytical. C 1s, F 1s, and S 2p spectra were collected and analyzed with CasaXPS software. Fourier-transform infrared (FT-IR) spectra were collected using Nicolet 6700 Fourier transform infrared spectrometer. Raman spectra were collected with a Renishaw inVia upright microscope using a 532 nm source. X-ray diffraction (XRD) patterns were collected with Rigaku MiniFlex II using Cu $K\alpha$ radiation.

Electrochemical Characterization: To measure the ionic conductivity, SSE film was cut and placed in a 10 mm PEEK die and pressed at 370 MPa for 3 min with titanium plungers. Electrochemical impedance spectroscopy (EIS) measurements were performed with an applied potential of 30 mV from 7 MHz to 1 Hz using Bio-Logic VSP-300. The obtained data were fitted with Z-View software. To obtain the electrochemical window of PTFE, AB and PTFE were first mixed at a weight ratio of 8:2 with a mortar and a pestle. Later, cyclic voltammetry (CV) was measured using PTFE-AB | LPSCI | Li and AB | LPSCI | Li cells at a scan rate of 0.1 mV s^{-1} over a voltage range of 0–4.3 V (vs Li/Li $^{+}$) using Bio-Logic VSP-300. DC polarizations were collected using the Solartron SI 1287 Potentiostat by applying a 0.5 V bias potential for 10 min.

Electrochemical Performance: Cathode composite was prepared by mixing NCM811 (1C = 200 mA h g^{-1}), ball-milled LPSCI, and VGCF with a weight ratio of 66:31:3 in a mortar and pestle for 30 min. To fabricate the cell, three layers of SSE films (≈ 75 mg) were punched into a 10 mm PEEK die with a titanium plunger and initially pressed at 310 MPa for 10 s. For the bilayer configuration, one layer of 0.2% PTFE and two layers of 0.5% PTFE SSE films were used. Afterward, 14.9 mg of cathode composite was placed into one side of the die and evenly spread using a titanium plunger. For the Li half-cell, the cell (SSE-cathode composite) was pressed at 370 MPa for 3 min, and Li metal was placed into the other side that was further pressed at 25 MPa for 30 min. For Si full-cell, Si anode (1C = 3500 mA h g^{-1}) with an N/P (negative to positive capacity) ratio of 1.2 (≈ 0.85 mg cm^{-2} of Si and ≈ 12.5 mg cm^{-2} of NCM811) was placed into the other side, and the cell (anode-SSE-cathode composite) was pressed

at 370 MPa for 3 min. The cell cycling was done under stack pressures of 5 and 75 MPa for Li and Si anodes, respectively, over the voltage range of 2.5–4.25 V using a Neware Battery cycler at room temperature.

Supporting Information

Supporting Information is available from the Wiley Online Library or from the author.

Acknowledgements

This work was supported by LG Energy Solution–U.C. San Diego Frontier Research Laboratory (FRL) via the Open Innovation program. This work was performed in part at the San Diego Nanotechnology Infrastructure (SDNI) of U.C. San Diego, a member of the National Nanotechnology Coordinated Infrastructure, which is supported by the National Science Foundation (Grant ECCS-1542148). This work was partially performed by the National Science Foundation through the U.C. San Diego Materials Research Science and Engineering Center (UCSD MRSEC, DMR-2011924) and National Science Foundation Materials Research Science and Engineering Center program through the U.C. Irvine Center for Complex and Active materials (DMR-2011967).

Conflict of Interest

The authors declare the following conflict of interest: Patents were filed for this work through UC San Diego's Office of Innovation and Commercialization and LG Energy Solution, Ltd.

Data Availability Statement

The data that support the findings of this study are available in the supplementary material of this article.

Keywords

all-solid-state batteries, dry process, polytetrafluoroethylene, solid-state electrolyte films

Received: February 5, 2023

Revised: March 4, 2023

Published online:

- [1] Y. S. Jung, D. Y. Oh, Y. J. Nam, K. H. Park, *Isr. J. Chem.* **2015**, *55*, 472.
- [2] A. Banerjee, X. Wang, C. Fang, E. A. Wu, Y. S. Meng, *Chem. Rev.* **2020**, *120*, 6878.
- [3] H. Kwak, S. Wang, J. Park, Y. Liu, K. T. Kim, Y. Choi, Y. Mo, Y. S. Jung, *ACS Energy Lett.* **2022**, *7*, 1776.
- [4] K. H. Park, Q. Bai, D. H. Kim, D. Y. Oh, Y. Zhu, Y. Mo, Y. S. Jung, *Adv. Energy Mater.* **2018**, *8*, 1800035.
- [5] T. Asano, A. Sakai, S. Ouchi, M. Sakaida, A. Miyazaki, S. Hasegawa, *Adv. Mater.* **2018**, *30*, 1803075.
- [6] Y. Kato, S. Hori, T. Saito, K. Suzuki, M. Hirayama, A. Mitsui, M. Yonemura, H. Iba, R. Kanno, *Nat. Energy* **2016**, *1*, 16030.
- [7] J. Jang, Y.-T. Chen, G. Deysner, D. Cheng, S.-Y. Ham, A. Cronk, P. Ridley, H. Yang, B. Sayahpour, B. Han, W. Li, W. Yao, E. A. Wu, J.-M. Doux, L. H. B. Nguyen, J. A. S. Oh, D. H. S. Tan, Y. S. Meng, *ACS Energy Lett.* **2022**, *7*, 2531.

- [8] D. H. S. Tan, Y.-T. Chen, H. Yang, W. Bao, B. Sreenarayanan, J.-M. Doux, W. Li, B. Lu, S.-Y. Ham, B. Sayahpour, J. Scharf, E. A. Wu, G. Deysher, H. E. Han, H. J. Hah, H. Jeong, J. B. Lee, Z. Chen, Y. S. Meng, *Science* **2021**, 373, 1494.
- [9] S. Ohno, W. G. Zeier, *Acc. Mater. Res.* **2021**, 2, 869.
- [10] Y.-G. Lee, S. Fujiki, C. Jung, N. Suzuki, N. Yashiro, R. Omoda, D.-S. Ko, T. Shiratsuchi, T. Sugimoto, S. Ryu, J. H. Ku, T. Watanabe, Y. Park, Y. Aihara, D. Im, I. T. Han, *Nat. Energy* **2020**, 5, 299.
- [11] J. Lee, S. H. Choi, G. Im, K. Lee, T. Lee, J. Oh, N. Lee, H. Kim, Y. Kim, S. Lee, J. W. Choi, *Adv. Mater.* **2022**, 34, 2203580.
- [12] A. Cronk, Y.-T. Chen, G. Deysher, S.-Y. Ham, H. Yang, P. Ridley, B. Sayahpour, L. H. B. Nguyen, J. A. S. Oh, J. Jang, D. H. S. Tan, Y. S. Meng, *ACS Energy Lett.* **2023**, 8, 827.
- [13] D. H. S. Tan, E. A. Wu, H. Nguyen, Z. Chen, M. A. T. Marple, J.-M. Doux, X. Wang, H. Yang, A. Banerjee, Y. S. Meng, *ACS Energy Lett.* **2019**, 4, 2418.
- [14] S.-K. Jung, H. Gwon, S.-S. Lee, H. Kim, J. C. Lee, J. G. Chung, S. Y. Park, Y. Aihara, D. Im, *J. Mater. Chem. A* **2019**, 7, 22967.
- [15] R. Koerver, I. Aygün, T. Leichtweiß, C. Dietrich, W. Zhang, J. O. Binder, P. Hartmann, W. G. Zeier, J. Janek, *Chem. Mater.* **2017**, 29, 5574.
- [16] S.-Y. Ham, H. Yang, O. Nunez-cuacuas, D. H. S. Tan, Y.-T. Chen, G. Deysher, A. Cronk, P. Ridley, J.-M. Doux, E. A. Wu, J. Jang, Y. S. Meng, *Energy Storage Mater.* **2023**, 55, 455.
- [17] P. Albertus, V. Anandan, C. Ban, N. Balsara, I. Belharouak, J. Buettner-Garrett, Z. Chen, C. Daniel, M. Doeff, N. J. Dudney, B. Dunn, S. J. Harris, S. Herle, E. Herbert, S. Kalnaus, J. A. Libera, D. Lu, S. Martin, B. D. McCloskey, M. T. McDowell, Y. S. Meng, J. Nanda, J. Sakamoto, E. C. Self, S. Tepavcevic, E. Wachsman, C. Wang, A. S. Westover, J. Xiao, T. Yersak, *ACS Energy Lett.* **2021**, 6, 1399.
- [18] K. T. Kim, T. Y. Kwon, Y. S. Jung, *Curr. Opin. Electrochem.* **2022**, 34, 101026.
- [19] J. Lee, T. Lee, K. Char, K. J. Kim, J. W. Choi, *Acc. Chem. Res.* **2021**, 54, 3390.
- [20] D. H. S. Tan, Y. S. Meng, J. Jang, *Joule* **2022**, 6, 1755.
- [21] S. N. Bryntesen, A. H. Strømman, I. Tolstorebrov, P. R. Shearing, J. J. Lamb, O. S. Burheim, *Energies* **2021**, 14, 1406.
- [22] J. Li, J. Fleetwood, W. B. Hawley, W. Kays, *Chem. Rev.* **2022**, 122, 903.
- [23] L. Chen, X. Xie, J. Xie, K. Wang, J. Yang, *J. Appl. Electrochem.* **2006**, 36, 1099.
- [24] Y. J. Nam, D. Y. Oh, S. H. Jung, Y. S. Jung, *J. Power Sources* **2018**, 375, 93.
- [25] M. Yamamoto, Y. Terauchi, A. Sakuda, M. Takahashi, *Sci. Rep.* **2018**, 8, 1212.
- [26] D. H. S. Tan, A. Banerjee, Z. Deng, E. A. Wu, H. Nguyen, J.-M. Doux, X. Wang, J. Cheng, S. P. Ong, Y. S. Meng, Z. Chen, *ACS Appl. Energy Mater.* **2019**, 2, 6542.
- [27] W. D. Jung, M. Jeon, S. S. Shin, J.-S. Kim, H.-G. Jung, B.-K. Kim, J.-H. Lee, Y.-C. Chung, H. Kim, *ACS Omega* **2020**, 5, 26015.
- [28] N. Rippaus, P. Strobl, B. Stiaszny, T. Zinkevich, M. Yavuz, J. Schnell, S. Indris, H. A. Gasteiger, S. J. Sedlmaier, *J. Electrochem. Soc.* **2018**, 165, A3993.
- [29] A. Sakuda, K. Kuratani, M. Yamamoto, M. Takahashi, T. Takeuchi, H. Kobayashi, *J. Electrochem. Soc.* **2017**, 164, A2474.
- [30] Y.-T. Chen, M. Duquesnoy, D. H. S. Tan, J.-M. Doux, H. Yang, G. Deysher, P. Ridley, A. A. Franco, Y. S. Meng, Z. Chen, *ACS Energy Lett.* **2021**, 6, 1639.
- [31] Y. Liu, R. Zhang, J. Wang, Y. Wang, *iScience* **2021**, 24, 102332.
- [32] Y.-T. Chen, M. A. T. Marple, D. H. S. Tan, S.-Y. Ham, B. Sayahpour, W.-K. Li, H. Yang, J. B. Lee, H. J. Hah, E. A. Wu, J.-M. Doux, J. Jang, P. Ridley, A. Cronk, G. Deysher, Z. Chen, Y. S. Meng, *J. Mater. Chem. A* **2022**, 10, 7155.
- [33] X. Li, J. Liang, K. R. Adair, J. Li, W. Li, F. Zhao, Y. Hu, T.-K. Sham, L. Zhang, S. Zhao, S. Lu, H. Huang, R. Li, N. Chen, X. Sun, *Nano Lett.* **2020**, 20, 4384.
- [34] K. Lee, S. Kim, J. Park, S. H. Park, A. Coskun, D. S. Jung, W. Cho, J. W. Choi, *J. Electrochem. Soc.* **2017**, 164, A2075.
- [35] Y. Lu, C.-Z. Zhao, H. Yuan, J.-K. Hu, J.-Q. Huang, Q. Zhang, *Matter* **2022**, 5, 876.
- [36] Y. Li, Y. Wu, Z. Wang, J. Xu, T. Ma, L. Chen, H. Li, F. Wu, *Mater. Today* **2022**, 55, 92.
- [37] F. Hippauf, B. Schumm, S. Doerfler, H. Althues, S. Fujiki, T. Shiratsuchi, T. Tsujimura, Y. Aihara, S. Kaskel, *Energy Storage Mater.* **2019**, 21, 390.
- [38] J. Li, Y. Li, S. Zhang, T. Liu, D. Li, L. Ci, *Chem. Eng. J.* **2022**, 455, 140605.
- [39] W. Ji, X. Zhang, D. Zheng, H. Huang, T. H. Lambert, D. Qu, *Adv. Funct. Mater.* **2022**, 32, 2202919.
- [40] C. Wang, R. Yu, H. Duan, Q. Lu, Q. Li, K. R. Adair, D. Bao, Y. Liu, R. Yang, J. Wang, S. Zhao, H. Huang, X. Sun, *ACS Energy Lett.* **2022**, 7, 410.
- [41] Y. Li, Y. Wu, T. Ma, Z. Wang, Q. Gao, J. Xu, L. Chen, H. Li, F. Wu, *Adv. Energy Mater.* **2022**, 12, 2201732.
- [42] Z. Zhang, L. Wu, D. Zhou, W. Weng, X. Yao, *Nano Lett.* **2021**, 21, 5233.
- [43] G. Li, R. Xue, L. Chen, *Solid State Ionics* **1996**, 90, 221.
- [44] S. Wang, X. Zhang, S. Liu, C. Xin, C. Xue, F. Richter, L. Li, L. Fan, Y. Lin, Y. Shen, J. Janek, C.-W. Nan, *J. Materiomics* **2020**, 6, 70.
- [45] G. Park, Y. Park, J. Park, J. Lee, *RSC Adv.* **2017**, 7, 16244.
- [46] J. Jansta, F. P. Dousek, *Electrochim. Acta* **1973**, 18, 673.
- [47] F. P. Dousek, J. Jansta, *Electrochim. Acta* **1975**, 20, 1.
- [48] W. Liu, X. Huang, L. Guobao, Z. Wang, H. Huang, L. Zhonghua, R. Xue, L. Chen, *J. Power Sources* **1997**, 68, 344.
- [49] S. Sun, S. Myung, G. Kim, D. Lee, H. Son, M. Jang, E. Park, B. Son, Y.-G. Jung, U. Paik, T. Song, *J. Mater. Chem. A* **2020**, 8, 17229.
- [50] J. Piowarczyk, R. Jędrzejewski, D. Moszyński, K. Kwiatkowski, A. Niemczyk, J. Baranowska, *Polymers* **2019**, 11, 1629.
- [51] S. Shiraishi, H. Kurihara, H. Tsubota, A. Oya, Y. Soneda, Y. Yamada, *Electrochem. Solid-State Lett.* **2001**, 4, A5.